Intraseasonal variations of water vapor and cirrus clouds in the tropical upper troposphere

AUTHOR(S):

Eguchi, Nawo; Shiotani, Masato

CITATION:

Eguchi, Nawo ...[et al]. Intraseasonal variations of water vapor and cirrus clouds in the tropical upper troposphere. Journal of Geophysical Research: Atmospheres 2004, 109(D12): D12106.

ISSUE DATE:

2004-06-27

URL:

http://hdl.handle.net/2433/217236

JOURNAL OF GEOPHYSICAL RESEARCH, VOL. 109, D12106, doi:10.1029/2003JD004314, 2004

Intraseasonal variations of water vapor and cirrus clouds in the tropical upper troposphere

Nawo Eguchi[1]

Division of Ocean and Atmospheric Sciences, Graduate School of Environmental Earth Science, Hokkaido University, Sapporo, Japan

Masato Shiotani

Research Institute for Sustainable Humanosphere, Kyoto University, Uji, Japan

Received 1 November 2003; revised 21 March 2004; accepted 8 April 2004; published 25 June 2004.

[1] Space-time variations of tropical upper tropospheric water vapor and cirrus clouds associated with the intraseasonal oscillation (ISO) are investigated using data from the Microwave Limb Sounder (MLS) and the Cryogenic Limb Array Etalon Spectrometer (CLAES) on board the Upper Atmosphere Research Satellite (UARS). Composite moisture and meteorological fields based on five ISO events selected in two boreal winters (1991–1993) are analyzed using 20–80 day band-pass-filtered data. At 215 and 146 hPa, wet anomalies with frequent appearance of cirrus clouds exist over the convective system and move eastward from the Indian Ocean to the central Pacific, suggesting a direct effect of convective activity up to this level. At 100 hPa, however, the moisture field seems to be indirectly affected by convective activity through the dynamical response to the convective heating. Dry anomalies are observed over the Indian Ocean around the developing stage and over the eastern Pacific around the mature-to-decaying stage of the ISO. Cirrus clouds are frequently found over the cold region located to the east of the convective system. These structures around the tropopause level are closely related to the eastward moving Kelvin and Rossby wave responses to the convective heating with the equatorial cold anomaly and with the subtropical anticyclonic gyres. Between the two gyres the easterly wind blowing through the equatorial cold region may cause dehydration through cirrus formation when the convective system develops over the Indian Ocean and the western Pacific. As the northern gyre intensifies, tropical dry air is transported to the subtropical Pacific and eventually to the equatorial eastern Pacific. It is suggested that the temperature and flow variations due to the coupled Kelvin-Rossby wave structure play an important role in dehydrating air in the tropical and subtropical tropopause region. *INDEX TERMS:* 3362 Meteorology and Atmospheric Dynamics: Stratosphere/troposphere interactions; 3374 Meteorology and Atmospheric Dynamics: Tropical meteorology; 0368 Atmospheric Composition and Structure: Troposphere—constituent transport and chemistry; *KEYWORDS:* upper tropospheric water vapor, cirrus clouds, intraseasonal oscillation

Citation: Eguchi, N., and M. Shiotani (2004), Intraseasonal variations of water vapor and cirrus clouds in the tropical upper troposphere, *J. Geophys. Res.*, *109*, D12106, doi:10.1029/2003JD004314.

1. Introduction

[2] Water vapor in the tropical upper troposphere has been a focus of much interest in the terrestrial radiation budget and the stratospheric chemical balance [e.g., *Soden and Fu*, 1995; *Stratospheric Processes and Their Role in Climate* (SPARC), 2000]. In particular, it plays a principal role in cirrus cloud formation linked to the radiative balance and dehydration mechanism in the upper troposphere [e.g., *Ramanathan and Collins*, 1991; *Rosenfield et al.*, 1998]. From the viewpoint of stratosphere-troposphere exchange (STE) the tropical upper troposphere, including the tropopause region, is important because it is the primary region of entry of mass and chemical species to the stratosphere.

[3] There has been substantial discussion on the tropical tropopause region in relation to STE mechanisms [e.g., *Holton et al.*, 1995]. The tropopause was regarded as a sharp boundary, but more recently it has been recognized that there is a transition layer between the troposphere and the stratosphere; it is called the tropical tropopause layer (TTL). The TTL is supposed to be located between a few kilometers below and above the tropical tropopause

[1]Now at Research Institute for Sustainable Humanosphere, Kyoto University, Uji, Japan.

0148-0227/04/2003JD004314

defined by the cold point temperature (about 14–19 km) [e.g., *Highwood and Hoskins*, 1998]. In the TTL, dynamical and chemical properties of the atmosphere gradually change from tropospheric to stratospheric features. Several dehydration mechanisms in the TTL have been proposed, such as slow rising motion across the cold tropical tropopause accompanied by freeze drying [e.g., *Brewer*, 1949], overshooting convective turrets that penetrate the tropopause and dehydrate [e.g., *Danielsen*, 1982], horizontal transport through the cold region that causes dehydration to the saturation mixing ratio in the TTL [*Holton and Gettelman*, 2001], and buoyancy waves with vertical parcel displacement bringing about temperature perturbations to dehydrate through ice cloud formation [*Potter and Holton*, 1995]. No conclusive evidence has yet been presented that any of these mechanisms is dominant.

[4] The intraseasonal oscillation (ISO), also known as the Madden and Julian Oscillation (MJO), with a timescale of 30–60 days, is one of the most dominant phenomena in the tropical region [e.g., *Madden and Julian*, 1994]. The eastward moving convective system affects not only the temperature and wind fields but also the humidity field in the troposphere. Moreover, the MJO could have an influence on tropical STE. In early studies, *Madden and Julian* [1972] suggested the existence of an eastward propagating temperature perturbation at the tropopause in accordance with the MJO. *Parker* [1973] found zonal wind disturbances associated with the equatorial Kelvin wave around the tropopause, between 150 and 70 hPa, with a timescale of 25–40 days. Recently, significant roles of the equatorial Kelvin wave and the MJO on the tropical STE have been pointed out using analysis of balloon-borne observations [e.g., *Fujiwara et al.*, 1998].

[5] In spite of its importance, upper tropospheric water vapor has not been well observed. This is mostly because of the difficulty in making accurate measurements of extremely low water concentration by using conventional observation techniques. The Microwave Limb Sounder (MLS) on board the Upper Atmosphere Research Satellite (UARS) provided upper tropospheric water vapor data on a global scale for about 7 years, beginning in September 1991 [*Barath et al.*, 1993], albeit with rather coarse resolution and fairly low precision. Using this data set, the global view of upper tropospheric water vapor has been gradually established, at least on seasonal timescales [e.g., *Read et al.*, 2001]. However, there is still a lack of understanding about the distribution and variation of water vapor in the tropical upper troposphere on intraseasonal timescales.

[6] There are few studies investigating characteristics of the ISO in upper tropospheric water vapor using the UARS MLS Upper Tropospheric Humidity (UTH) data [*Clark et al.*, 1998; *Mote et al.*, 2000; *Sassi et al.*, 2002]. *Clark et al.* [1998] found an eastward moving moisture field associated with the MJO at 215 hPa in the tropics. *Mote et al.* [2000] examined the intraseasonal response of water vapor over convective systems, finding a change from anomalously wet conditions at 146 hPa to anomalously dry at 100 hPa in the Eastern Hemisphere. However, these studies have not necessarily addressed the mechanisms which control the water vapor distribution in the TTL associated with the ISO, which will be discussed in this study.

[7] Thin cirrus clouds have also been given attention from the viewpoint of dehydration around the tropopause. *Jensen et al.* [1996] proposed, using a detailed microphysical cloud model, that cirrus clouds near the tropical tropopause region can be classified into two types: anvil cirrus clouds from deep convection and in situ cirrus produced by large-scale slow upward motion. The latter mechanism is supported by an observation of thin cirrus layers far from deep convection [*Winker and Trepte*, 1998]. *Potter and Holton* [1995] proposed that thin ice clouds in the lower stratosphere can be generated by vertical parcel displacement produced by convectively driven buoyancy waves, using a mesoscale dynamical model with tropical convection to support this mechanism. The result also indicates that dehydration does not require convection to penetrate the tropopause. *Boehm and Verlinde* [2000] suggested, using lidar and radiosonde observations, that cirrus clouds near the tropopause are related to temperature perturbations owing to the equatorial Kelvin wave. However, the formation and maintenance of cirrus clouds near the tropopause on the global scale have not yet been clearly understood.

[8] Several investigations have been conducted with satellite observations on the seasonal and interannual variations of upper tropospheric cirrus clouds. *Wang et al.* [1996] inferred subvisual clouds in the upper troposphere and the lower stratosphere from the aerosol extinction data of the Stratospheric Aerosol and Gas Experiment (SAGE) II. They revealed that the derived cloud distribution is similar in space and time to the previous cirrus climatology determined from ground-based observations [*Warren et al.*, 1986, 1988]. They showed that the subvisual cloud frequency in the tropics is 45% in the zonal mean and 70% over the western Pacific in the annual mean data set.

[9] To infer the tropical upper tropospheric cirrus, *Mergenthaler et al.* [1999] tried to use the 780 cm^{-1} aerosol extinction data of the Cryogenic Limb Array Etalon Spectrometer (CLAES) on board UARS and compared their result with the SAGE II cloud climatology of *Wang et al.* [1996]. They regarded an extinction value (0.9×10^{-3} km^{-1}) as a threshold of thin cirrus clouds and found that the seasonal distribution of clouds derived from the CLAES agrees well with the SAGE II result.

[10] Moreover, *Sandor et al.* [2000] compared MLS relative humidity data (relative humidity with respect to ice; hereafter RHi) with cirrus clouds inferred from the CLAES aerosol data based on the same threshold as *Mergenthaler et al.* [1999]; the CLAES and the MLS measurements are coincident to less than 30 s, which corresponds to 200 km, along track. They found a strong correlation between the two data sets and showed that the cirrus clouds inferred from the MLS RHi exhibit clear interannual variations, such as those due to the El Niño/Southern Oscillation (ENSO) cycle.

[11] This study will focus on space-time variations of upper tropospheric water vapor and cirrus clouds associated with the ISO by using the UARS MLS water vapor data and the UARS CLAES aerosol data. In particular, we will investigate relationships among water vapor, cirrus clouds, and meteorological fields in the TTL and will try to find a

control mechanism of water vapor distribution in the TTL associated with the ISO.

[12] The analysis data are explained in section 2. We perform a composite analysis on water vapor mixing ratio, cirrus cloud frequency, and meteorological variables, which is explained in detail in section 3. In section 4 we show longitudinal characteristics of moisture and other fields during the ISO life cycle by using the composite data. We also investigate the vertical features in section 5 and the horizontal structures in section 6. Finally, section 7 summarizes and concludes the findings.

2. Data

[13] We used the UARS MLS water vapor data in the upper troposphere (level 2, version 490) and in the lower stratosphere (level 3AT, version 0104) [cf. *Read et al.*, 2001; *Pumphrey*, 1999]. The MLS on board the UARS observed the low latitudes (30°S–30°N) from October 1991 to April 1993 with only a few gaps. The MLS views the atmospheric limb in a perpendicular direction to the orbit path and yields a total of about 1300 vertical profiles along the orbit each day with adjacent orbits being separated by about 25°.

[14] A daily grid map of water vapor used in this study is constructed by the following procedure. First, all profile data of the ascending and descending nodes for each day are binned into the corresponding longitude-latitude box on a 5° × 2.5° grid. Since there are too few data to cover the globe for each day, we composited data from 5 days to define each daily map rather than doing interpolation in the longitudinal direction. Then we can use an almost complete grid of data between 30°S and 30°N from October 1991 to April 1993.

[15] The upper tropospheric data for relative humidity with respect to ice (RHi, %) and water vapor mixing ratio by volume (hereafter WVm, ppmv) are provided at the UARS standard pressure levels [cf. *Read et al.*, 2001], but in the lower stratosphere (above 100 hPa) only the WVm data are provided. In the tropics, pressure levels at 215, 146, and 100 hPa almost correspond to 11.5, 14.0, and 16.5 km, respectively. The level at 146 hPa is close to the bottom of the TTL; most tropical convection can reach up to this level [cf. *Gettelman et al.*, 2001].

[16] The MLS UTH data contain an artifact related to the UARS yaw cycle about every 36 days, especially at 146 hPa [cf. *Read et al.*, 2001]. The yaw cycle variation of brightness measured by the MLS is about 0.8 K, which corresponds to about 10 ppmv variation of WVm at 146 hPa. This effect is not obvious at 215 and 100 hPa. To avoid this effect, we use departures from the zonal mean for the composite analysis at all levels. Anomalies from the zonal mean are also used for other meteorological parameters. Thus we will not discuss the zonally uniform structure of temperature field in the tropical upper troposphere such as that reported by *Bantzer and Wallace* [1996].

[17] The MLS often provided values over 100% RHi in the tropical upper troposphere. The fraction of data over 100% RHi at 146 hPa reaches nearly 80% over the active convective areas, such as Africa, South America, the maritime continent, and the western Pacific. This is supposed to be due to retrieval issues affected by several factors, such as random error and uncertainty in the National Centers for Environmental Prediction (NCEP) temperatures, but *Jensen et al.* [1999] presumed that an existence of ice particles in the field of limb viewing with about 200 km would be the most critical one. They further showed that high humidity in the MLS data is closely related to frequent occurrence of cirrus clouds in the tropical tropopause region. In this study, all values greater than 100% RHi are replaced with 100% RHi.

[18] As described in section 1, it has been known that cirrus clouds inferred from the CLAES aerosol data can well represent the cirrus climatology [*Mergenthaler et al.*, 1999] and that the cirrus cloud frequency is in good agreement with the high RHi frequency of the MLS [*Jensen et al.*, 1999; *Sandor et al.*, 2000]. In this study we used the current version 9 CLAES 780 cm^{-1} aerosol extinction data to detect ice particles. The version 9 data set is a recommended version for use, but we found that distribution of the version 9 extinction data is rather different from that of the version 8 data used by *Mergenthaler et al.* [1999]. After comparing with the MLS RHi data over 100%, which can be statistically regarded as cirrus clouds at 146 hPa, we set a new threshold to be 3.3×10^{-3} km^{-1} rather than 0.9×10^{-3} km^{-1} which was used by *Mergenthaler et al.* [1999].

[19] Other meteorological variables such as temperature and wind fields come from the European Centre for Medium-Range Weather Forecasts (ECMWF) operational analysis data. The ECMWF data are available on a 2.5° × 2.5° grid, but we reduced the longitude grid to 5° interval and interpolated the data onto the UARS standard levels in the log-pressure coordinate.

[20] Outgoing longwave radiation (OLR) data come from the National Oceanic and Atmospheric Administration (NOAA) operational satellites. The OLR is used as a proxy for the intensity of convection. The daily interpolated OLR data are available on a 2.5° × 2.5° grid, but we reduced these data to a 5° × 2.5° grid.

3. Filtering Process and Composite Procedure

[21] The primary focus of this study is on temporal and spatial variability of the upper tropospheric water vapor and cirrus clouds with an intraseasonal timescale. To isolate the ISO signal, we applied a 20–80 day band-pass Lanczos filter with 201 weights to all variables. The exception is for the cirrus cloud frequency, since it has a bounded value between 0 and 100%.

[22] Figure 1 shows a longitude-time section of the OLR anomaly field averaged between 10°S and 10°N. Some eastward moving convective systems are evident from the Indian Ocean to the western Pacific, particularly during boreal winter and spring. Convective activity in the Eastern Hemisphere is larger than that in the Western Hemisphere. We focus on ISO events during boreal winter seasons when the eastward propagating feature is clearly seen [e.g., *Madden*, 1986] and when dehydration in the TTL is supposed to be most effective since the tropopause temperature in the boreal winter is colder than that in the boreal summer [*Seidel et al.*, 2001]. We calculated the standard deviation at each grid point with the band-pass-

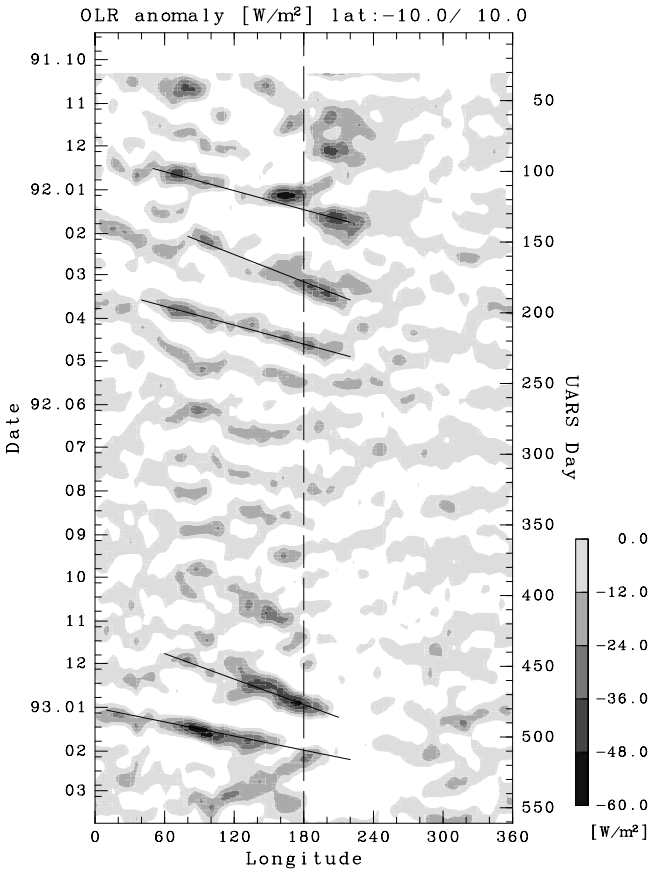

Figure 1. Longitude-time section of the band-pass-filtered OLR anomaly field averaged between 10°S and 10°N. Negative values are shaded. Five solid lines indicate the selected intraseasonal events.

filtered OLR data between 30°S and 30°N during boreal winter (from November to April) and found the maximum at 165°E, 10°S; we define this location as a reference point. The next maximum exists over the equatorial Indian Ocean where most intraseasonal convection develops [*Wang and Rui*, 1990].

[23] The time series of OLR anomalies at the reference point is used as an index of the ISO. Following *Kiladis et al.* [2002], the day having the lowest OLR anomaly value under −20 W m^{-2} is referred as day 0 (the key day). Five ISO events are selected on the basis of this index. A track for each convective system is subjectively superimposed with a solid line in Figure 1. Although each event has different features, such as about the propagation speed and intensity, the composite OLR field well represents a typical ISO life cycle, as will be shown in section 4.

[24] During the El Niño winters, convective activity related to the MJO penetrates more eastward into the central Pacific than normal [e.g., *Fink and Speth*, 1997; *Hendon et al.*, 1999]. Note that the first winter is in a developing stage of the 1991–1992 ENSO event when the central eastern Pacific is warmer than usual and the active convective region shifts eastward. The latter two events are included in the period of Tropical Ocean Global Atmospheres/ Coupled Ocean Atmosphere Response Experiment of the Intensive Observation Period: November 1992 to February 1993 (TOGA/COARE IOP), and there are some studies investigating these events in detail [e.g., *Yanai et al.*, 2000].

4. Characteristics of Eastward Propagating System

4.1. OLR and Velocity Potential

[25] Figure 2 shows a longitude-time section of the composite OLR anomaly (contours) and the velocity potential anomaly at 146 hPa (shading) averaged between 10°S and 10°N. Open circles indicate the location of the OLR minimum on each day. In the OLR field the active convective region appears over the central Indian Ocean around day −20 and moves eastward to the date line with an average phase speed of 5.4 m s^{-1}, which is in good agreement with previous studies [e.g., *Hendon and Salby*, 1994]. After passing over the date line, convective activity decays, and the eastward moving system is hardly observed in the Western Hemisphere.

[26] In the velocity potential field at 146 hPa (shading in Figure 2), negative anomalies move around the globe. In the Eastern Hemisphere from the Indian Ocean to the western Pacific the minimum values are almost constant, and locations of these minima correspond approximately to those of the OLR minima. In the Western Hemisphere, though the negative anomalies are weak, they move eastward faster than in the Eastern Hemisphere. The period of the eastward moving system around the globe is about 45 days.

4.2. Temperature and Zonal Wind

[27] Figure 3 shows longitude-time sections of the composite temperature and zonal wind anomaly fields at 100, 146, and 215 hPa. Open circles represent the location of the OLR minimum on each day, indicating the active convection center as in Figure 2.

[28] At 215 hPa (Figure 3c) an area of divergence is located slightly to the east side of the convective center and moves eastward from the Indian Ocean to the central Pacific. Warm anomalies (red contours) with an amplitude of about 2 K precede the active convective system by about 20°. This feature in the temperature field is similar to that found by *Hendon and Salby* [1994]. Consequently, the warm anomalies precede the easterly wind anomalies by

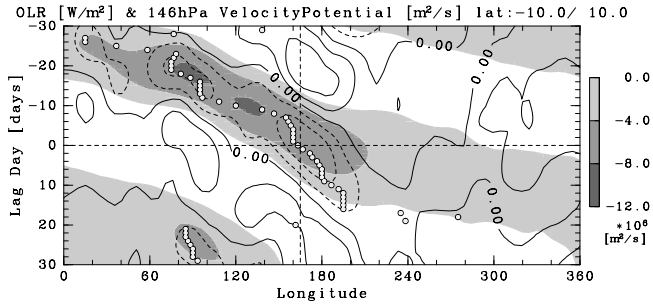

Figure 2. Longitude-time section of composite OLR (W m^{-2}, contours) and velocity potential (m^2 s^{-1}) at 146 hPa (shading) averaged between 10°S and 10°N. Contour intervals are 9.0 W m^{-2}. Open circles indicate location of the minimum OLR at each day. Negative values are shaded.

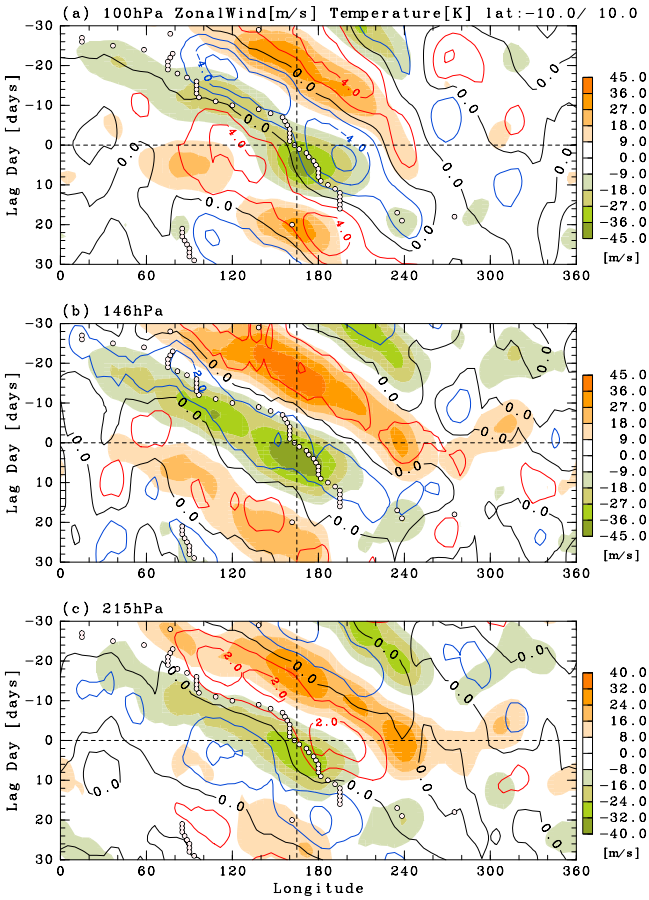

Figure 3. Longitude-time sections of zonal wind (m s^{-1}, shading) and temperature (K, contours) at (a) 100 hPa, (b) 146 hPa, and (c) 215 hPa. Red (blue) contours are warm (cold) anomalies. Black contours indicate zero. Contour intervals are 1.0, 1.0, and 2.0 K at 215, 146, and 100 hPa, respectively. Open circles show location of the minimum OLR at each day.

about 35°, indicating that the temperature anomalies and the zonal wind anomalies are almost in quadrature.

[29] At 146 hPa (Figure 3b) the easterly (westerly) wind anomalies are in phase with the cold (warm) anomalies from the Indian Ocean to the central Pacific. At 100 hPa (Figure 3a), cold anomalies with an amplitude of about 5 K appear at about 30° on the east side of the convective system. The cold anomalies precede the easterly wind anomalies which are located almost over the convection center, indicating that the temperature anomalies and the zonal wind anomalies are almost in quadrature, but the phase relation is opposite to that at 215 hPa. This is because the temperature anomalies tilt eastward with increasing altitude (see Figure 6), though the zonal wind anomalies are almost coherent in the vertical direction. The temperature structure is regarded as the Kelvin wave response to convective heating [e.g., *Hendon and Salby*, 1994].

4.3. Water Vapor and Temperature

[30] Next we show longitude-time sections of the composite WVm field with the temperature field superimposed at 100, 146, and 215 hPa to clarify relationships between the two parameters (Figure 4). At 215 hPa (Figure 4c), wet anomalies (blue shading) move eastward with the convective system from the Indian Ocean to the western Pacific. Temporal variability of WVm anomalies is larger in the Eastern Hemisphere, especially over the western Pacific with an amplitude of about 30 ppmv, than in the Western Hemisphere where the eastward propagating anomaly is hardly seen.

[31] At 146 hPa (Figure 4b) in the Eastern Hemisphere the wet anomalies still exist over the convective system, and they move eastward accordingly. A correlation between the temperature and WVm anomalies at 146 hPa is negative. Around day 0, dry anomalies appear over the eastern Pacific, which may be related to the corresponding anomaly at 100 hPa seen in Figure 4a. The water vapor distribution at 146 hPa seems to be affected from below and above.

[32] At 100 hPa (Figure 4a) the eastward moving humidity field is not clear. Over the Indian Ocean the dry anomalies (purple shading) appear around day −14, and the wet anomalies appear around day +8. Over the Pacific Ocean, on the contrary, the wet anomalies appear around day −14, and the dry anomalies appear around day +5. This nonpropagating dipole feature of the WVm anomalies at 100 hPa will be discussed in detail

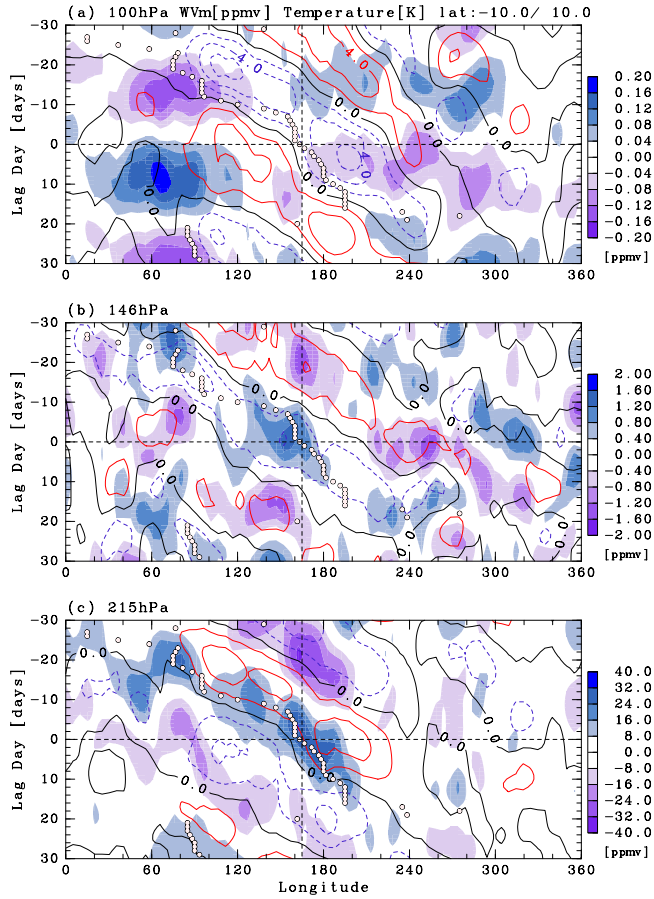

Figure 4. Same as Figure 3 but for water vapor mixing ratio (ppmv, shading) and temperature (K, contours).

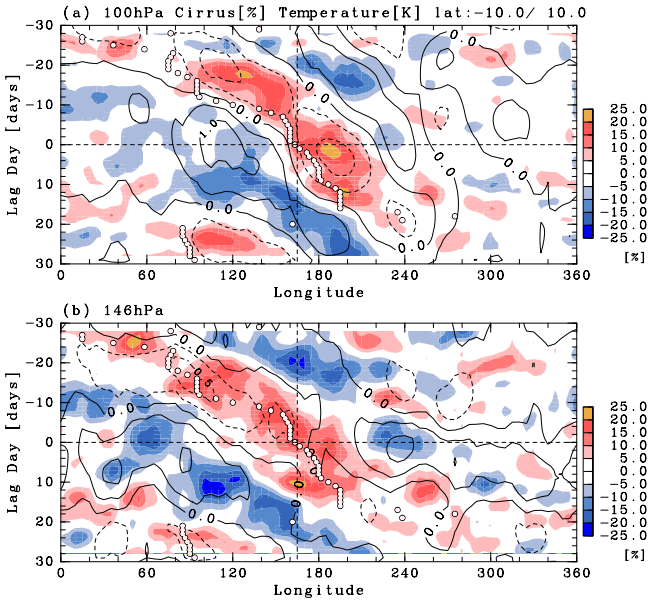

Figure 5. Same as Figure 3 but for cirrus cloud frequency (%) at (a) 100 hPa and (b) 146 hPa (shading) using the composed data without the band-pass filter.

later (Figure 7) in relation to the horizontal transport of dry air.

4.4. Cirrus Cloud Frequency

[33] Figure 5 shows longitude-time sections of cirrus cloud frequency anomalies at 100 and 146 hPa inferred from the CLAES aerosol data averaged between 10°S and 10°N. No result is shown at 215 hPa, since the CLAES measurement is degraded by overlying clouds, especially over the convective region [*Mergenthaler et al.*, 1999]. As described in section 3, we used the zonal and temporal anomaly data to show the space-time development of cirrus clouds. The cirrus cloud frequency averaged over the convective area is about 60% at 100 hPa and 70% at 146 hPa. Eastward moving positive anomalies of the cloud frequency at 146 hPa coexist with the cold anomalies where the convective system is active (Figure 4b).

[34] At 100 hPa (Figure 5a), positive anomalies of the cloud frequency still coexist with the cold anomalies at the east side of the convective system from the Indian Ocean to the central Pacific. In particular, higher cirrus cloud frequencies coincide with the cold temperatures at 120°E on day −18 and at 180°E on day +2 when the convective system is active, suggesting a clear relationship between the cirrus cloud occurrence and the cold temperature.

5. Vertical Structures

[35] In this section, we describe the vertical structure of WVm and other meteorological variables to summarize the relationship shown in section 4. Figure 6 shows longitude-pressure cross sections of the composite anomalies of WVm (shading), cirrus cloud frequency (triangles), temperature (contours), and wind fields (vectors) averaged between 10°S and 10°N on day −15 and day 0, representing a developing and a mature stage of the ISO, respectively. The ISO indices for the 2 days are almost in an opposite phase, and the convective centers on each day are located at 110°E and 165°E, respectively. Around the convective center, strong ascent and wet anomalies are seen throughout the troposphere.

[36] For the temperature field on both days, warm anomalies exist slightly to the east side of the convective system in the middle troposphere up to around 215 hPa, with its maximum located around 300 hPa. At 146 and 100 hPa, cold anomalies appear over the convective region. On days −15 and 0, the minimum temperature at 100 hPa is located at 125°E and 190°E, respectively. The vertical structure tilts eastward with increasing height above 215 hPa; thus the temperature anomaly changes sign around 200 hPa, as already shown in Figure 4. This feature is essentially similar to that due to the convectively coupled Kelvin wave [e.g., *Wheeler et al.*, 2000; *Straub and Kiladis*, 2003]. The existence of the cold anomalies near the tropopause over the convective clouds is also reported by *Johnson and Kriete* [1982]. In the wind field on both days, upward motion is dominant over the convective system at 215 and 146 hPa, and the easterly anomalies prevail at 100 hPa.

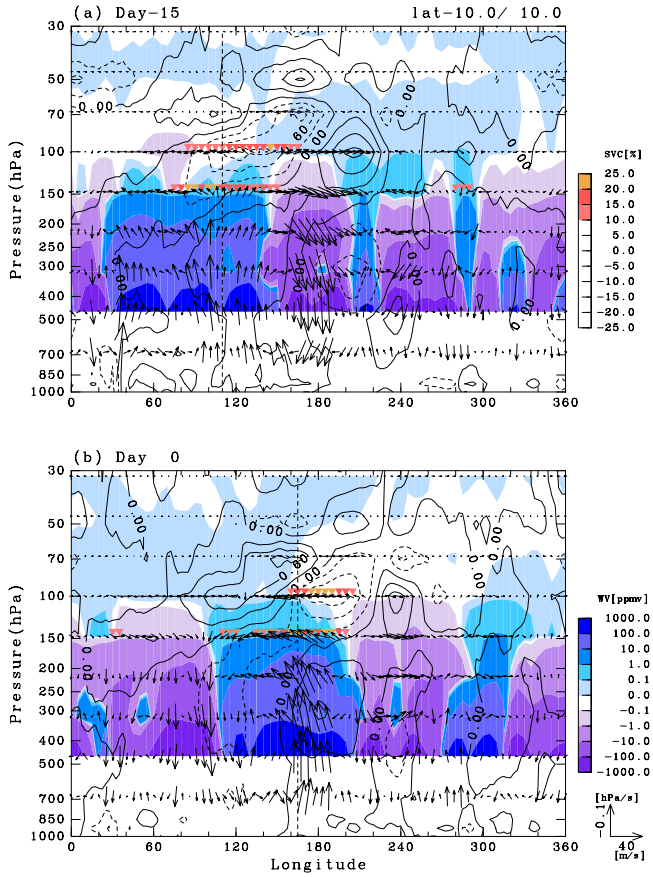

Figure 6. Longitude-pressure sections of water vapor (ppmv, shading), cirrus cloud frequency (%, triangles), temperature (K, contours), and zonal (m s^{-1}) and vertical (hPa s^{-1}) wind components (vectors) averaged between 10°S and 10°N on (a) day −15 and (b) day 0. Contour intervals are 0.3 K. Vertical broken lines at 110°E on day −15 and at 165°E on day 0 indicate the convective centers.

[37] On day 0, wet anomalies (about 10 ppmv) extend up to 146 hPa over the convective region; at 100 hPa, dry anomalies exist at the east side of the convective system, where it is cold. On day −15, overall features of the WVm field are similar to those on day 0 up to 146 hPa, but the dry anomalies are located at the west side of the convective system (about 80°E) at 100 hPa. This discrepancy at 100 hPa will be discussed later in Figure 7.

[38] On both days at 146 hPa, cirrus clouds occur frequently over the convective system with the wet and cold anomalies, but those at 100 hPa occur frequently in the cold anomalies ahead of the convective system. It should be noted again that the temperature structure and the resulting cirrus cloud occurrence around the tropical tropopause are strongly controlled by the Kelvin wave response to the convective heating with the ISO timescales. It is well known that the convective heating can also produce characteristic flow patterns due to the Rossby wave response, and the related horizontal features will be described in section 6.

6. Horizontal Structures at 100 hPa

[39] Figure 7 shows horizontal maps at 100 hPa from day −15 to day +5 every 5 days to view the influence of the meteorological fields on water vapor and cirrus cloud distributions. Figure 7 uses the composite data without applying the band-pass filter or subtracting the zonal mean.

[40] Figure 7a shows the wind field and the saturation WVm field inferred from the ECMWF temperature. The convective center (minimum in OLR) indicated by a red star is located over Indonesia on day −15 when the ISO is developing. On day −10 it moves to the Timor Sea, and the minimum OLR anomaly weakens (see Figure 2 and *Rui and Wang* [1990] and *Yanai et al.* [2000]). The convective system becomes stronger again around day −5 when it moves to the western Pacific, and it becomes a mature stage on day 0 around 165°E, 7.5°S. On day +5 the convective center moves over the central Pacific, and afterward, the OLR anomaly diminishes.

[41] In the saturation WVm field in Figure 7a, low values (cold regions) are seen over the western and central Pacific. The main structure is almost quasi-stationary throughout the period and symmetric with respect to the equator. The WVm of 3 ppmv (dark shading) corresponds to the temperature of 189.6 K at 100 hPa. The strength and longitudinal extent of the cold region vary with the eastward moving convective system. When convective activity becomes larger around day −15 (more exactly day −18) and day 0, the temperature gets colder over the western and central Pacific, respectively (see also Figure 3). This suggests that the effective dehydration may occur around this time.

[42] In the wind field, eastward moving anticyclonic gyres located at the northwest and southwest of the cold region are prominent; the northern one is stronger than the southern one, as shown by *Kiladis et al.* [2001]. The easterly over the equatorial cold region is a part of the anticyclonic gyres, and the divergent area is located at the east side of the coldest region. In the northern subtropics, there are strong westerlies (20 ∼ 30 m s^{-1}), and they are coupled with the northern subtropical gyre. The wind field is also modulated by the ISO as in the temperature field. On day −15 the wind field is rather zonal, and the easterly at the west side of the cold region reaches Africa. Between day −10 and day −5 the easterly diminishes in the Indian Ocean, but the southerly becomes stronger (about 7 m s^{-1}) over the South China Sea and the western Pacific, as the northern gyre develops. The center of the northern gyre further moves eastward to 180°E on day 0. Through the period the southern gyre is not clearer than the northern one. Consequently, the coupled structure of the cold region and the gyres moves eastward with the convective system.

[43] Figure 7b shows the composite WVm and the cirrus cloud frequency. The WVm minima are mostly found along two latitude circles, one over the equator and the other around 25°N. There exist high cirrus cloud frequency regions over the western and central Pacific, Africa, and South America, along the equator where it is cold. Around days −15 and 0 the cirrus clouds occur frequently over the western and central Pacific, respectively, as shown in Figure 5a. The Southern Hemisphere is about 1 ppmv wetter than the Northern Hemisphere, which is also shown by *Gettelman et al.* [2002] using WVm averaged over eight Januaries (1992–1999) of the Halogen Occultation Experiment (HALOE) data. They suggested that the wetter air is provided by deep convection which is located in the south of the equator in January. Our results suggest that the northern gyre makes it much drier in the Northern Hemisphere than in the Southern Hemisphere.

[44] Time variations of the WVm distribution are closely coupled with the temperature and the wind fields. On day −15, dry regions are found around the equator and 25°N from the Indian Ocean to the eastern Pacific. On day −10 a bridge of a dry airstream is established around 70°E between the two dry latitude bands in association with the development of the subtropical northern gyre. On day −5 the bridge in the Eastern Hemisphere moves eastward, and another bridge is established in the eastern Pacific. On day 0 the western bridge is diminishing, and the dry region is found in the equatorial central and eastern Pacific. The latter seems to be a pond of dry air transported along the dry stream from the equator and through the subtropics. On day +5 the dry region in the northern subtropics becomes weak, but it remains over the equatorial central and eastern Pacific. The sequence of the WVm variations suggests that the gyres contribute to dehydration through the equatorial cold region and to an exchange of the dry air between the tropics and the subtropics.

[45] Subtropical dry air moves eastward faster than that in the equatorial region since the subtropical westerly is faster than the eastward propagating speed of the convective system. In a longitude-time section of WVm in the northern subtropics (Figure 8) it is clear that the dry region moves eastward around the globe, but it is less clear over the central Indian Ocean (day −15) and the eastern Pacific (day 0). Around these days in the equatorial region (see Figure 4a) the dry anomalies appear and extend westward around day −15 and eastward and westward after day 0, respectively. The eastward moving dry anomalies are not clear around these days because the dry air created over

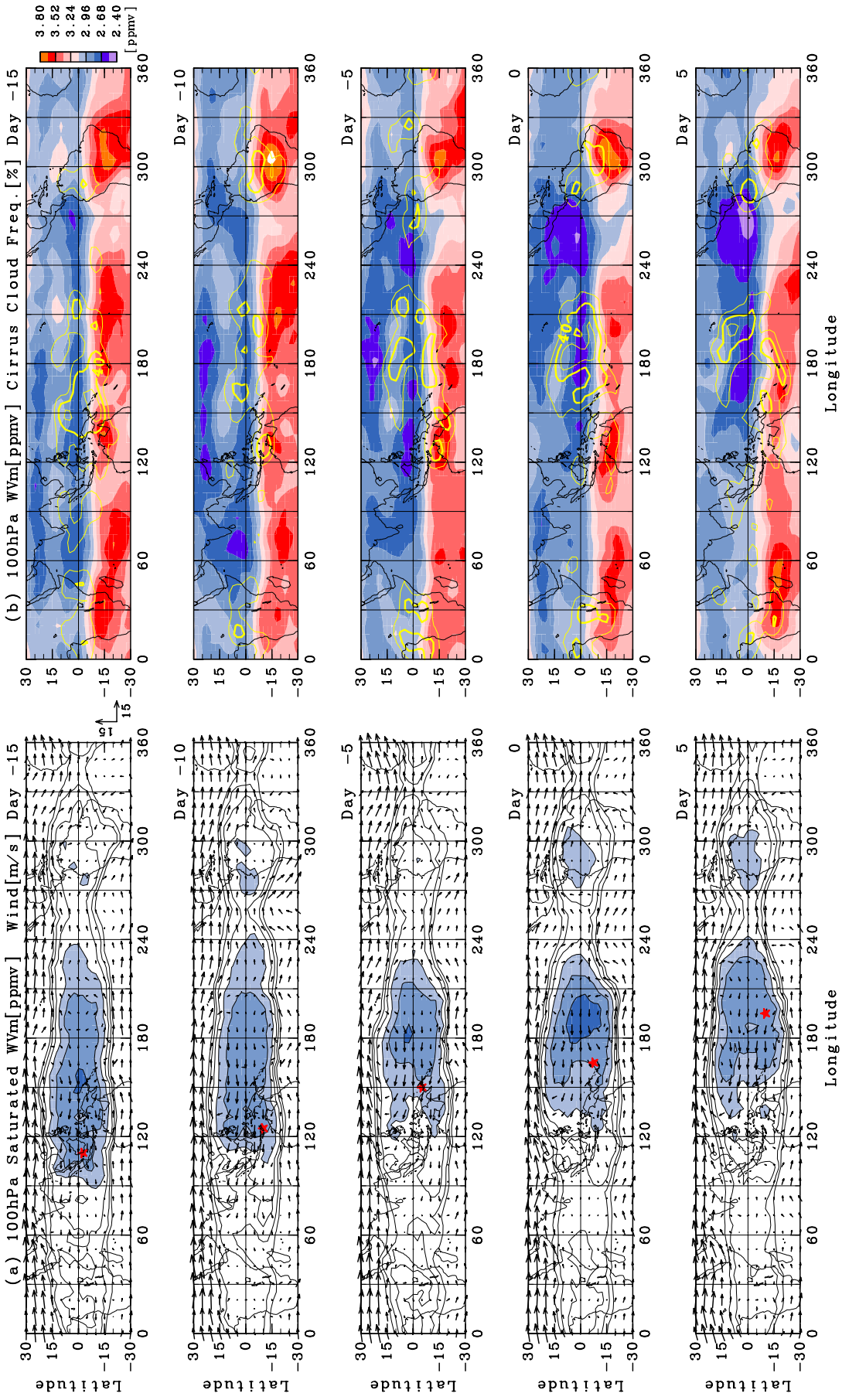

Figure 7. Longitude-latitude sections of (a) saturation mixing ratio from temperature (ppmv, contours and shading) and horizontal wind components (m s^{-1}, vectors) at 100 hPa and (b) water vapor mixing ratio (ppmv, shading) and cirrus cloud frequency (contours) from day −15 to day +5 every fifth day. In Figure 7a a red star indicates the convective center on each day. Contour intervals are 1.0 ppmv. Light blue indicates less than 5.0 ppmv. Dark blue indicates less than 3.0 ppmv. In Figure 7b, contour intervals start from 20% with an interval of 20%.

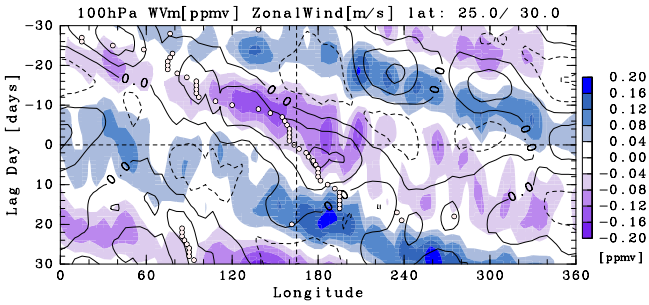

Figure 8. Same as Figure 4a, but contours indicate zonal wind (m s^{-1}) at 100 hPa averaged between 25°N and 30°N. Contour intervals are 10.0 m s^{-1}. Open circles show location of the minimum OLR at each day in the equatorial region (10°S–10°N).

the equatorial cold region is transported to the subtropics by the northern gyre, which enhances when the convective system moves eastward over the Pacific.

7. Summary and Conclusions

[46] We have investigated space-time variations of tropical upper tropospheric water vapor and cirrus clouds associated with the ISO, such as the MJO, by using the WVm and cirrus cloud frequency data from the UARS MLS and CLAES. The five ISO events during boreal winter (November–April) from October 1991 to April 1993 are composited with respect to the time series at the reference point (165°E, 10°S) where variations of the OLR anomalies are largest.

[47] The wet anomalies at 215 hPa lie over the convective region and move eastward with an average phase speed of 5.4 m s^{-1} from the Indian Ocean to the date line. After passing the date line, the convective system decays, and the wet anomalies disappear. At 146 hPa the moisture and cirrus cloud fields move eastward with the convective system within the Eastern Hemisphere as at 215 hPa. It is suggested that the WVm distributions up to this level are strongly affected by convective activity. At 100 hPa the eastward moving system of the WVm anomalies is not clearly seen in the tropics. Cirrus clouds occur frequently in the cold anomalies located in the east side of the convective system. It is suggested that cirrus clouds around the tropopause are formed because of cold temperature induced by the convective system.

[48] Dynamical structures in the TTL associated with the ISO seem to be due to a combination of the equatorial Kelvin wave response around the equator and the equatorial Rossby wave response in the tropics and subtropics [e.g., *Rui and Wang*, 1990; *Hendon and Salby*, 1994; *Matthews*, 2000; *Straub and Kiladis*, 2003]. The temperature field is almost symmetric with respect to the equator and tilts eastward with increasing height in the tropics; this would be due to the equatorial Kelvin wave response. At 100 hPa the minimum temperature is located over the equator at the east side of the convective system, where cirrus clouds occur frequently. The cirrus cloud occurrence is closely related to the temperature perturbation associated with the ISO.

[49] Two gyres linked to the Rossby wave response are seen to the northwest and southwest of the cold region. At 100 hPa, air may be dried through cirrus formation when it passes through the cold region over the equator along the easterly wind between the two gyres. The dried air is conveyed to the subtropics, and some of it returns to the equatorial region. It is suggested that the Northern Hemisphere is much drier because the northern gyre is stronger than the southern one. Thus the gyres may affect dehydration around the cold region and exchange between the tropics and subtropics.

[50] *Fujiwara et al.* [1998, 2001] proposed the role of the equatorial Kelvin wave in dehydrating air entering the lower stratosphere, but the discussion is limited only to the equatorial region. *Hatsushika and Yamazaki* [2003] investigated a dehydration mechanism in the TTL by using an atmospheric general circulation model with a mean steady flow during boreal winter and showed that the anticyclonic gyres over the tropical western Pacific entrain air several times to the equatorial cold region. Observationally, *Pfister et al.* [2001] found from a back trajectory calculation during boreal winter that advection linked to the anticyclonic circulation over the western Pacific can transport dry air dehydrated over the equatorial cold region. Synthesizing these previous works, the present study has shown using satellite data that the intraseasonal variations of the easterly wind linked to the Rossby wave response over the cold region linked to the Kelvin wave response could play a central role in dehydration in the TTL.

[51] The analysis period includes the warm phase of the ENSO (1991–1992 El Niño). The meteorological fields are affected by the convective perturbation associated with the ENSO [e.g., *Yulaeva and Wallace*, 1994]. During El Niño winters the MJO events intrude into the central Pacific [e.g., *Hendon et al.*, 1999]. Comparing the composite WVm field of the first two events during 1991–1992 boreal winter with one of the last two events during 1992–1993 boreal winter, the dry region appears from the Indian Ocean to the eastern Pacific in the former but from the Indian Ocean to the western Pacific in the latter (not shown). However, the main features of the temperature and wind fields are commonly seen in the five ISO events.

[52] Distribution of the averaged WVm at 100 hPa during the boreal winter is shown by *Gettelman et al.* [2002] using the HALOE data. They found that the WVm minimum located at the northern subtropics is caused by the meridional transport associated with the local Hadley circulation through the cold region. They also showed that cirrus clouds inferred from the HALOE aerosol data occur frequently over the cold region, similar to Figure 7. Comparing the horizontal distribution of the averaged MLS WVm during the boreal winter seasons (December, January, and February in 1991–1993, similar to Figure 7b) with Figure 1 of *Gettelman et al.* [2002], the most striking difference is that the dry regions along the equator can only be seen in the MLS data. The discrepancy may suggest the difference between the HALOE and the MLS measurements. The vertical field of view of the 183 GHz band which is used to retrieve the stratospheric water vapor is nearly 4 km at 100 hPa. Since the averaging kernel for 100 hPa WVm has a peak close to 68 hPa [*Pumphrey*, 1999], the WVm data at

100 hPa may be affected by the upper layer. Probably because of this reason, WVm at 100 hPa is about 0.5 ppmv drier than the HALOE observation in the tropics [*Pumphrey et al.*, 2000]. The validation with other instruments is discussed in detail by *Read et al.* [2001, 2004].

[53] Further understanding of the intraseasonal WVm variation and the effect of the ISO on the dehydration mechanism around the tropopause region is required. We hope that the new MLS and other instruments on board the Earth Observing System (EOS) Aura, which will be launched in 2004, provide extensive measurements of water vapor, cirrus clouds, and other minor species and that we utilize these data to clarify the variation of water vapor around the TTL in much detail.

[54] **Acknowledgments.** We would like to thank Koji Yamazaki, Masatomo Fujiwara, Hiroaki Hatsushika, Andrew Gettelman, and one anonymous reviewer for their critical comments and valuable suggestions. We would also like to thank Timothy J. Dunkerton, Philip Mote, and Steven Pawson, who provided very useful comments for this study. We thank Masanori Niwano for providing the HALOE data. We also thank the UARS MLS science staffs, especially William G. Read and Dong Liang Wu. We acknowledge the UARS CLAES science team, the European Centre for Medium-Range Weather Forecasts (ECMWF) and the National Oceanic and Atmospheric Administration (NOAA) OLR data product for the data sets. Most of the figures in this study were drawn through use of the GFD-DENNOU Library.

References

Bantzer, C. H., and J. M. Wallace (1996), Intraseasonal variability in tropical mean temperature and precipitation and their relation to the tropical 40–50 day oscillation, *J. Atmos. Sci.*, *53*, 3032–3045.

Barath, F. T., et al. (1993), The Upper Atmosphere Research Satellite Microwave Limb Sounder instrument, *J. Geophys. Res.*, *98*(D6), 10,751–10,762.

Boehm, M. T., and J. Verlinde (2000), Stratospheric influence on upper tropospheric tropical cirrus, *Geophys. Res. Lett.*, *27*(19), 3209–3213.

Brewer, A. W. (1949), Evidence for a world circulation provided by the measurements of helium and water vapour distribution in the stratosphere, *Q. J. R. Meteorol. Soc.*, *75*, 351–363.

Clark, H. L., R. S. Harwood, P. W. Mote, and W. G. Read (1998), Variability of water vapor in the tropical upper troposphere as measured by the Microwave Limb Sounder on UARS, *J. Geophys. Res.*, *103*(D24), 31,695–31,707.

Danielsen, E. F. (1982), A dehydration mechanism for the stratosphere, *Geophys. Res. Lett.*, *9*(6), 605–608.

Fink, A., and P. Speth (1997), Some potential forcing mechanisms of the year-to-year variability of the tropical convection and its intraseasonal (25–70 day) variability, *Int. J. Climatol.*, *17*, 1513–1534.

Fujiwara, M., K. Kita, and T. Ogawa (1998), Stratosphere-troposphere exchange of ozone associated with the equatorial Kelvin wave as observed with ozonesondes and rawinsondes, *J. Geophys. Res.*, *103*(D15), 19,173–19,182.

Fujiwara, M., F. Hasebe, M. Shiotani, N. Nishi, H. Vömel, and S. J. Oltmans (2001), Water vapor control at the tropopause by equatorial Kelvin waves observed over the Galapagos, *Geophys. Res. Lett.*, *28*(16), 3142–3146.

Gettelman, A., W. J. Randel, S. Massie, F. Wu, W. G. Read, and J. M. Rusell III (2001), El-Niño as a natural experiment for studying the tropical tropopause region, *J. Clim.*, *14*, 3375–3392.

Gettelman, A., W. J. Randel, F. Wu, and S. T. Massie (2002), Transport of water vapor in the tropical tropopause layer, *Geophys. Res. Lett.*, *29*(1), 1009, doi:10.1029/2001GL013818.

Hatsushika, H., and K. Yamazaki (2003), Stratospheric drain over Indonesia and dehydration within the tropical tropopause layer diagnosed by air parcel trajectories, *J. Geophys. Res.*, *108*(D19), 4610, doi:10.1029/2002JD002986.

Hendon, H., and M. L. Salby (1994), The life cycle of the Madden-Julian Oscillation, *J. Atmos. Sci.*, *51*, 2225–2237.

Hendon, H., C. Zhang, and J. D. Glick (1999), Interannual variation of the Madden-Julian Oscillation during austral summer, *J. Clim.*, *12*, 2538–2550.

Highwood, E. J., and B. J. Hoskins (1998), The tropical tropopause, *Q. J. R. Meteorol. Soc.*, *124*, 1579–1604.

Holton, J. R., and A. Gettelman (2001), Horizontal transport and the dehydration of the stratosphere, *Geophys. Res. Lett.*, *28*(14), 2799–2802.

Holton, J. R., P. H. Harnes, M. E. McIntyre, A. R. Douglass, R. B. Rood, and L. Pfister (1995), Stratosphere-troposphere exchange, *Rev. Geophys.*, *33*(4), 403–439.

Jensen, E. J., O. B. Toon, H. B. Selkirl, J. D. Spinhirne, and M. R. Schoeberl (1996), On the formation and persistence of subvisible cirrus clouds near the tropical tropopause, *J. Geophys. Res.*, *101*(D16), 21,361–21,375.

Jensen, E. J., W. G. Read, J. Mergenthaler, B. J. Sandor, L. Pfister, and A. Tabazadeh (1999), High humidities and subvisible cirrus near the tropical tropopause, *Geophys. Res. Lett.*, *26*(15), 2347–2350.

Johnson, R. H., and D. C. Kriete (1982), Thermodynamic and circulation characteristics of winter monsoon tropical mesoscale convection, *Mon. Weather Rev.*, *110*(12), 1898–1911.

Kiladis, G. N., K. H. Straub, G. C. Reid, and K. S. Gage (2001), Aspects of interannual and intraseasonal variability of the tropopause and lower stratosphere, *Q. J. R. Meteorol. Soc.*, *127*, 1961–1983.

Kiladis, G. N., D. J. Seidel, and K. H. Straub (2002), Variability of the tropical tropopause, *SPARC Newsl.*, *18*, 18–22.

Madden, R. A. (1986), Seasonal variations of the 40–50 day oscillation in the tropics, *J. Atmos. Sci.*, *43*, 3138–3158.

Madden, R. A., and P. R. Julian (1972), Description of global-scale circulation scales in the tropics with a 40–50 day period, *J. Atmos. Sci.*, *29*, 1109–1123.

Madden, R. A., and P. R. Julian (1994), Observations of the 40–50-day tropical oscillation: A review, *Mon. Weather Rev.*, *122*(5), 814–837.

Matthews, A. J. (2000), Propagation mechanisms for the Madden-Julian Oscillation, *Q. J. R. Meteorol. Soc.*, *126*, 2637–2652.

Mergenthaler, J. L., A. E. Roche, J. B. Kumer, and G. A. Ely (1999), Cryogenic Limb Array Etalon Spectrometer observations of tropical cirrus, *J. Geophys. Res.*, *104*(D18), 22,183–22,194.

Mote, P. W., H. L. Clark, T. J. Dunkerton, R. S. Harwood, and H. C. Pumphrey (2000), Intraseasonal variations of water vapor in the tropical upper troposphere and tropopause region, *J. Geophys. Res.*, *105*(D13), 17,457–17,470.

Parker, D. E. (1973), Equatorial Kelvin waves at 100 millibars, *Q. J. R. Meteorol. Soc.*, *99*, 116–129.

Pfister, L., et al. (2001), Aircraft observations of thin cirrus clouds near the tropical tropopause, *J. Geophys. Res.*, *106*(D9), 9765–9786.

Potter, B. E., and J. R. Holton (1995), The role of monsoon convection in the dehydration of the lower tropical stratosphere, *J. Atmos. Sci.*, *52*, 1034–1050.

Pumphrey, H. C. (1999), Validation of a new prototype water vapor retrieval for the UARS Microwave Limb Sounder, *J. Geophys. Res.*, *104*(D8), 9399–9412.

Pumphrey, H. C., H. L. Clark, and R. S. Harwood (2000), Lower stratospheric water vapor measured by UARS MLS, *Geophys. Res. Lett.*, *27*(12), 1691–1694.

Ramanathan, V., and W. Collins (1991), Thermodynamic regulation of ocean warming by cirrus clouds deduced from observations of the 1987 El Niño, *Nature*, *351*, 27–32.

Read, W. G., et al. (2001), UARS Microwave Limb Sounder upper tropospheric humidity measurement: Method and validation, *J. Geophys. Res.*, *106*(D23), 32,207–32,258.

Read, W. G., D. L. Wu, J. W. Waters, and H. C. Pumphrey (2004), A new 147–56 hPa water vapor product from the UARS Microwave Limb Sounder, *J. Geophys. Res.*, *109*, D06111, doi:10.1029/2003JD004366.

Rosenfield, J. E., D. B. Considine, M. R. Schoeberl, and E. D. Browell (1998), The impact of subvisible cirrus clouds near the tropical tropopause on stratospheric water vapor, *Geophys. Res. Lett.*, *25*(11), 1883–1886.

Rui, H., and B. Wang (1990), Development characteristics and dynamic structure of tropical intraseasonal convection anomalies, *J. Atmos. Sci.*, *47*, 357–379.

Sandor, B. J., E. J. Jensen, E. M. Stone, W. G. Read, J. W. Waters, and J. L. Mergenthaler (2000), Upper tropospheric humidity and thin cirrus, *Geophys. Res. Lett.*, *27*(17), 2645–2648.

Sassi, F., M. Salby, H. C. Pumphrey, and W. Read (2002), Influence of the Madden-Julian Oscillation on upper tropospheric humidity, *J. Geophys. Res.*, *107*(D23), 4681, doi:10.1029/2001JD001331.

Seidel, D. J., R. J. Ross, J. K. Angell, and G. C. Reid (2001), Climatological characteristics of the tropical tropopause as revealed by radiosondes, *J. Geophys. Res.*, *106*(D8), 7857–7878.

Soden, B. J., and R. Fu (1995), A satellite analysis of deep convection, upper tropospheric humidity, and the greenhouse effect, *J. Clim.*, *8*, 2333–2351.

Stratospheric Processes and their Role in Climate (SPARC) (2000), Assessment of upper tropospheric and lower stratospheric water vapor, *WCRI*

113, *WMO/TD-N0 1043*, edited by D. Kley, J. M. Russell III, and C. Phillips, World Meteorol. Org., Geneva, Switzerland.

Straub, K. H., and G. N. Kiladis (2003), The observed structure of convectively coupled Kelvin waves: Comparison with simple models of coupled wave instability, *J. Atmos. Sci.*, *60*, 1655–1668.

Wang, B., and H. Rui (1990), Synoptic climatology of transient tropical intraseasonal convection anomalies, *Meteorol. Atmos. Phys.*, *44*, 43–61.

Wang, P. H., P. Minnis, P. McCormick, G. S. Kent, and K. M. Skeens (1996), A 6-year climatology of cloud occurrence frequency from Stratospheric Aerosol and Gas Experiment II observations (1985–1990), *J. Geophys. Res.*, *101*(D23), 29,407–29,429.

Warren, S. G., C. J. Hahn, J. London, R. M. Chervin, and R. L. Jenne (1986), Global distribution of total cloud cover and cloud type amounts over land, *NCAR Tech. Note TN-273*, 29 pp., Natl. Cent. for Atmos. Res., Boulder, Colo.

Warren, S. G., C. J. Hahn, J. London, R. M. Chervin, and R. L. Jenne (1988), Global distribution of total cloud cover and cloud type amounts over the ocean, *NCAR Tech. Note TN-317*, 42 pp., Natl. Cent. for Atmos. Res., Boulder, Colo.

Wheeler, M., G. N. Kiladis, and P. J. Webster (2000), Large-scale dynamical fields associated with convectively coupled equatorial waves, *J. Atmos. Sci.*, *57*, 613–640.

Winker, D. M., and C. R. Trepte (1998), Laminar cirrus observed near the tropical tropopause by LITE, *Geophys. Res. Lett.*, *25*(17), 3351–3354.

Yanai, M., B. Chen, and W. W. Tung (2000), The Madden-Julian Oscillation observed during the TOGA COARE IOP: Global view, *J. Atmos. Sci.*, *57*, 2374–2396.

Yulaeva, E., and J. M. Wallace (1994), The signature of ENSO in global temperature and precipitation fields derived from the Microwave Sounding Unit, *J. Clim.*, *7*, 1719–1736.

N. Eguchi and M. Shiotani, Research Institute for Sustainable Humanosphere (RISH), Kyoto University, Gokasho, Uji, Kyoto, 611-0011, Japan. (nawo@rish.kyoto-u.ac.jp; shiotani@rish.kyoto-u.ac.jp)